Green Chemistry

PAPER

View Article Online
View Journal | View Issue

Cite this: *Green Chem.*, 2024, **26**, 11924

Engineering *in situ*: N-doped porous carbon-confined FeF_3 for efficient lithium storage†

Jinlong Hu,[a] Weijun Xu‡[a,b] and Lingzhi Zhang *[a,b]

Metal fluorides confined in heteroatom-doped carbon nanostructures are viewed as one of the most promising high capacity cathodes for high-performance lithium rechargeable batteries. Herein, we present a facile *in situ* reaction approach to synthesize nitrogen-doped porous carbon (NPC)-confined metal fluorides, which involves *in situ* etching toward a Schiff-base organic precursor and fluorination of metal oxides by polytetrafluoroethylene during a one-step heating process. The afforded NPC-confined FeF_3 (FeF_3@NPC) facilitates fast Li^+/e^- diffusion kinetics, accommodates severe volume fluctuation and reduces the FeF_3 cathode dissolution, thus providing an outstanding high-rate capacity of 181 mA h g^{-1} at 5 C, accompanied by superior cycle life within 500 cycles at 2 C. This novel approach opens up new horizons to design high-performance nanoconfined metal fluoride-based materials for sustainable energy applications.

Received 16th August 2024,
Accepted 22nd October 2024

DOI: 10.1039/d4gc04097j

rsc.li/greenchem

Introduction

Lithium-metal fluoride batteries have attracted intensive research interest for prospective next-generation electrochemical energy-storage devices owing to their high theoretical energy density and operating voltage.[1] In recent years, lots of studies have been focused on revealing the reaction mechanisms and optimizing the electrochemical properties of metal fluoride cathodes (FeF_3, CoF_2, and CuF_2).[2,3] Compared to Co and Cu, Fe possesses more abundant resources, and eco-friendly and low-cost properties. In addition, FeF_3, as a typical member of the metal fluorides, has impressive advantages in terms of the considerable theoretical capacity (712 mA h g^{-1}), energy density (1500 W h L^{-1}), and high average potential (~2.74 V), which are conducive to future large-scale applications.[4–6] Despite these appealing features, the commercialization of Li-FeF_3 batteries is seriously hindered by multiple challenges, including the highly insulating electronic/ionic characteristics of FeF_3, the significant volumetric change upon delithiation/lithiation, and the dissolution of FeF_3 during cycling, which inevitably lead to limited high-rate capability and poor long-term cyclability.[7–9]

To circumvent the aforementioned challenges, numerous purposeful efforts have been committed to designing and preparing nanostructured conductive carbon matrices that serve as the coating or carrier of FeF_3, such as mesoporous carbon, carbon spheres, heteroatom-doped carbon, carbon nanotubes, and graphene.[10–15]

Among a variety of carbons, heteroatom-doped carbon nanostructures containing confined FeF_3 have impressive merits: (i) carbon frameworks can improve the conductivity of FeF_3; (ii) confined carbon-coated space can tolerate the volumetric changes of active materials; (iii) nano-confinement can reduce the metal fluoride cathode dissolution during cycling to some extent; and (iv) heteroatom doping can boost the lithium storage performance of FeF_3 owing to additional active sites for metal ion storage.[16,17] Nevertheless, the synthesis of nanoconfined heteroatom-doped carbon-coated FeF_3 usually involves complicated synthetic processes and toxic/corrosive gases (*e.g.*, HF and NF_3).[18–20] More importantly, deriving from *ex situ* synthesis methods, the conductive contact between FeF_3 and carbon matrices is quite weak. Thus, developing a simple, *in situ* engineering approach without using toxic/corrosive gases to prepare nanoconfined heteroatom-doped carbon-coated FeF_3 is highly desirable.

In this contribution, we propose a general approach for *in situ* synthesis of nitrogen-doped porous carbon-confined metal fluorides (*e.g.*, FeF_3@NPC, CoF_2@NPC, CuF_2@NPC, and AlF_3@NPC), by a straightforward heating treatment using a Schiff-base organic precursor (SOP) as a carbon, nitrogen, and template agent source, metal oxides as metal precursors, and

[a]*CAS Key Laboratory of Renewable Energy, Guangdong Provincial Key Laboratory of New and Renewable Energy Research and Development, Guangzhou Institute of Energy Conversion, Chinese Academy of Sciences, Guangzhou 510640, Guangdong, China. E-mail: lzzhang@ms.giec.ac.cn*
[b]*School of Energy Science and Engineering, University of Science and Technology of China, Hefei 230026, Anhui, China*

†Electronic supplementary information (ESI) available: SEM images, EDS, XRD, Raman, TGA and tables of calculation results. See DOI: https://doi.org/10.1039/d4gc04097j

‡These authors contributed equally to this work.

polytetrafluoroethylene (PTFE) as an etching and fluorinating agent. In a well-constructed FeF_3@NPC nanocomposite, a nitrogen-doped micro/mesoporous carbon shell surrounding the FeF_3 nanoparticles enables good nanoconfinement ability, ideal conductive contact, high pore volume space, and suitable active sites for the FeF_3 electrode, bringing about superior electrochemical performance. This novel strategy offers the possibility to design multifunctional carbon-confined metal fluoride materials in a facile, environmentally benign, and controllable way for efficient lithium rechargeable batteries.

Results and discussion

Fig. 1a illustrates *in situ* synthesis toward FeF_3@NPC, involving a Schiff-base reaction between 3-aminopropyltriethoxysilane (APTES) and glutaraldehyde ($C_5H_8O_2$) to generate SOP-encapsulated Fe_2O_3 (Fe_2O_3@SOP), followed by heating treatment to obtain FeF_3@NPC. During the heating process, PTFE can completely decompose at 606 °C to produce tetrafluoroethylene gas (C_2F_4) (Fig. S1†),[21] which will fluorinate Fe_2O_3 into FeF_3 and react with Si/O elements of SOP to etch the SOP template, forming N-doped porous carbon-confined FeF_3. As shown in SEM and TEM images (Fig. 1b–d), Fe_2O_3@SOP shows an interconnected spheroidal morphology, with a spheroidal size of around 40–120 nm, and the pristine Fe_2O_3 nanoparticles (Fig. S2†) are encapsulated within the SOP. After heating Fe_2O_3@SOP, for the as-prepared FeF_3@NPC, the morphology and spheroidal size are similar to those of Fe_2O_3@SOP, except that the Fe_2O_3 nanoparticles and SOP are transformed into FeF_3 nanoparticles and porous carbon, respectively (Fig. 1e/f). *In situ* formed carbon layers are uniformly coated surrounding the FeF_3, and the lattice fringe spacing of 0.37 nm can be ascribed to the (110) plane of the FeF_3 phase (Fig. 1g/h).[11] The elemental mappings of FeF_3@NPC (Fig. 1i) show the homogeneous distribution of Fe, F, C, O and N elements and the overlapped F and Fe signals surrounded by the C signal. The extremely weak Si peak (0.53 at% for the residual Si content)

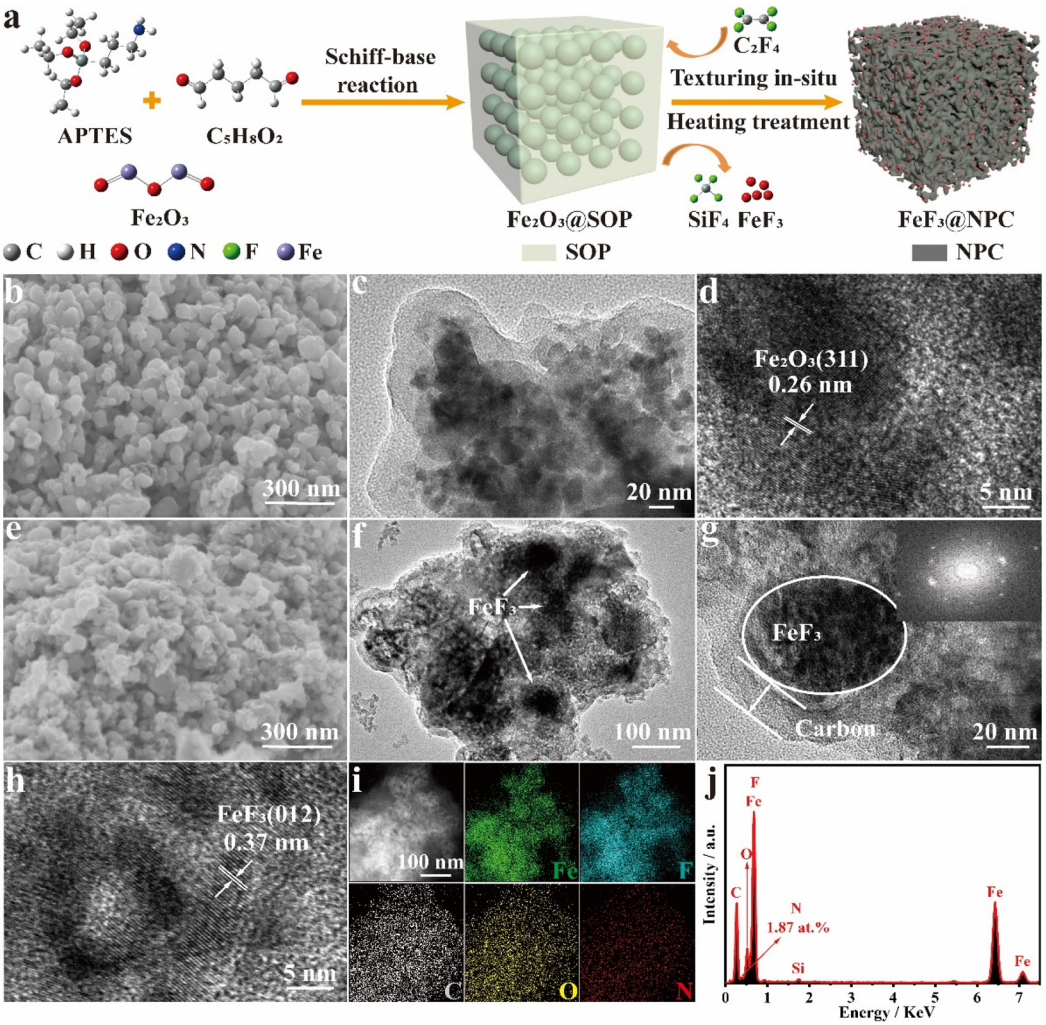

Fig. 1 (a) Schematic illustration of FeF_3@NPC synthesis. (b) SEM, (c) TEM, and (d) HRTEM images of Fe_2O_3@SOP. (e) SEM image, (f and g) TEM images, (h) HRTEM image, (i) STEM and corresponding elemental mappings, and (j) EDX spectrum of FeF_3@NPC.

suggests the removal of Si in the SOP, and the N doping content in the FeF_3@NPC is found to be 1.87 at% (Fig. 1j).

The diffraction peaks of FeF_3@NPC are clearly indexed to FeF_3 (JCPDS No. 33-0647) (Fig. 2a), suggesting the successful conversion of Fe_2O_3 into FeF_3. In the FTIR spectra of FeF_3@NPC (Fig. 2b), the peaks at 539 and 1265 cm^{-1} correspond to the stretching vibrations of Fe–F and C–N, respectively,[15,22] further indicating the formation of FeF_3 and N doping of the carbon framework. The Raman spectrum of FeF_3@NPC exhibits two intense peaks appearing at approximately 1361 cm^{-1} (D-band) and 1581 cm^{-1} (G-band) (Fig. S3†). The intensity ratio (I_D/I_G) is 1.01, implying that there are abundant structural defects in the FeF_3@NPC,[23] thus favoring Li^+ transfer kinetics.[24] The electrical conductivity of FeF_3@NPC evaluated by a four-point probe technique is 0.56 S cm^{-1}, which is higher than that of pure FeF_3 (2.53×10^{-9} S cm^{-1}),[25] demonstrating the enhanced conductivity of FeF_3 with a N-doped porous carbon coating. The constituent element state occurring in FeF_3@NPC was investigated by XPS (Fig. 2c), showing the presence of C, F, Fe, C, N, and O. The Fe 2p spectrum (Fig. 2d) exhibits Fe 2p1/2 and Fe 2p3/2 peaks appearing at 728.8 and 714.9 eV, and their respective satellite peaks located at 721.1 and 710.1 eV, respectively, indicating that the Fe species in the FeF_3@NPC are expressed as Fe^{3+} valence states. The typical bonding type at 685.9 eV of the F 1s spectrum (Fig. 2e) corresponds to the F–Fe^{3+} bonds,[26] further proving the formation of FeF_3. The N 1s spectrum (Fig. 2f) shows three peaks corresponding to graphitic N, pyridinic N, and pyrrolic N, which is conducive to enhancing the electronic conductivity and active material absorbability of the carbon matrix.[27,28] The C 1s spectrum (Fig. 2g) shows four evident peaks corresponding to C–C, C–N/C–O, O–C=O, and C–F,[29] where the former three can be ascribed to carbonization of SOP, and the fourth is caused by the slight fluorination of carbon. The N_2 sorption analysis of FeF_3@NPC presents hierarchical micro–mesoporous structures, which is affirmed using pore-size distribution (Fig. 2h).[24,30] Two different kinds of pores are created from the *in situ* concurrent PTFE-based etching and fluorination. The specific surface area of FeF_3@NPC is determined to be as high as 167.1 m^2 g^{-1}, together with the pore volume of 0.32 cm^3 g^{-1}. The air-exposed TGA curve of FeF_3@NPC shows a mass loss between 50 and

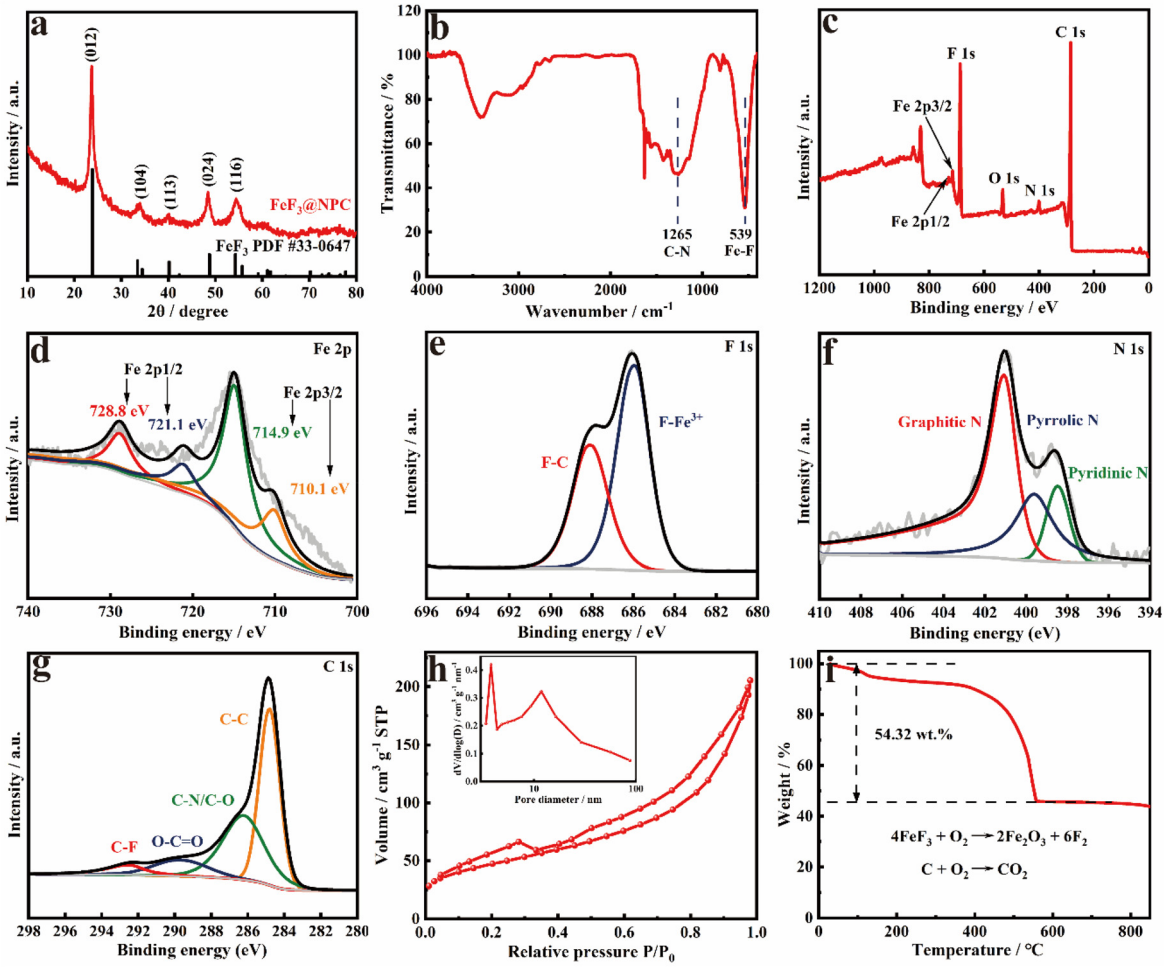

Fig. 2 (a) XRD patterns, (b) FTIR spectra, (c) XPS survey spectrum, (d) Fe 2p, (e) F 1s, (f) N 1s and (g) C 1s XPS spectra, (h) N_2 sorption isotherm and pore size distribution, and (i) TGA curve in air of FeF_3@NPC.

800 °C (Fig. 2i), demonstrating that the residue (Fe_2O_3) at 800 °C is 54.32 wt%. Accordingly, it is determined that the content of FeF_3 in FeF_3@NPC is 64.55 wt%.

The effects of the mass ratio of PTFE to Fe_2O_3@SOP and heat treatment temperature on the formation of FeF_3@NPC were explored. As the mass ratio of PTFE/Fe_2O_3@SOP decreases from 6 : 1 to 3 : 1, the interconnected spheroidal morphology remains unchanged (Fig. 3a/b), but Si in the SOP cannot be completely etched, which can be shown by EDS analysis (Fig. 3c). On increasing the mass ratio of PTFE/Fe_2O_3@SOP to 10 : 1, the interconnected spheroidal shape collapses and the carbon content increases (Fig. 3d–f), implying a decrease of the active substance FeF_3. Thus, PTFE is critical for creating a nanoconfined spheroidal carbon shell and tuning the FeF_3 content. Increasing the heating temperature to 800 °C, the spheroidal FeF_3@NPC nanoparticles are aggregated into a blocky morphology (Fig. 3g/h), which indicates that a higher heating temperature affects the regular morphology of FeF_3@NPC. To further explore the formation of FeF_3@NPC, TG and gas emission curves of the PTFE and Fe_2O_3@SOP mixture were constructed. The TG curve (Fig. S4†) shows that PTFE and Fe_2O_3@SOP react violently at around 580 °C, which can be attributed to the fluorination of Fe_2O_3 based on the major gas product (C_2F_4) of PTFE in the pyrolysis process and the etching of Si in the SOP through the reaction of Si with C_2F_4 to generate SiF_4 (g) (Fig. 3i),[24,31] resulting in the formation of FeF_3@NPC.

The successful synthesis of FeF_3@NPC has inspired us to explore the possibility of utilizing the *in situ* reaction approach in the preparation of other N-doped porous carbon-confined metal fluorides. Indeed, as seen in the SEM images and XRD patterns shown in Fig. 4, CoF_2@NPC, CuF_2@NPC, and AlF_3@NPC can be easily synthesized using common metal oxides such as Co_3O_4, Cu_2O and Al_2O_3, respectively, which can be further supported by the EDS spectra of CoF_2@NPC, CuF_2@NPC, and AlF_3@NPC (Fig. S5–7†).

To systematically assess the electrochemical properties of FeF_3@NPC, FeF_3@NPC/Li cells with an FeF_3@NPC cathode were constructed. The CV profiles of the FeF_3@NPC cathode in the initial cathodic sweep show a pair of cathodic/anodic peaks at 2.93/3.15 V (Fig. 5a), which correspond to lithiation/delithiation of the FeF_3 crystal structure, respectively.[32,33] An additional pair of cathodic/anodic peaks at 3.28/3.40 V is exhibited, relating to the redox reactions of Li^+ with FeF_3 to form the $Li_{0.5}FeF_3$ intermediate.[34] The cathodic/anodic peaks are almost overlapped during the subsequent cycles, implying

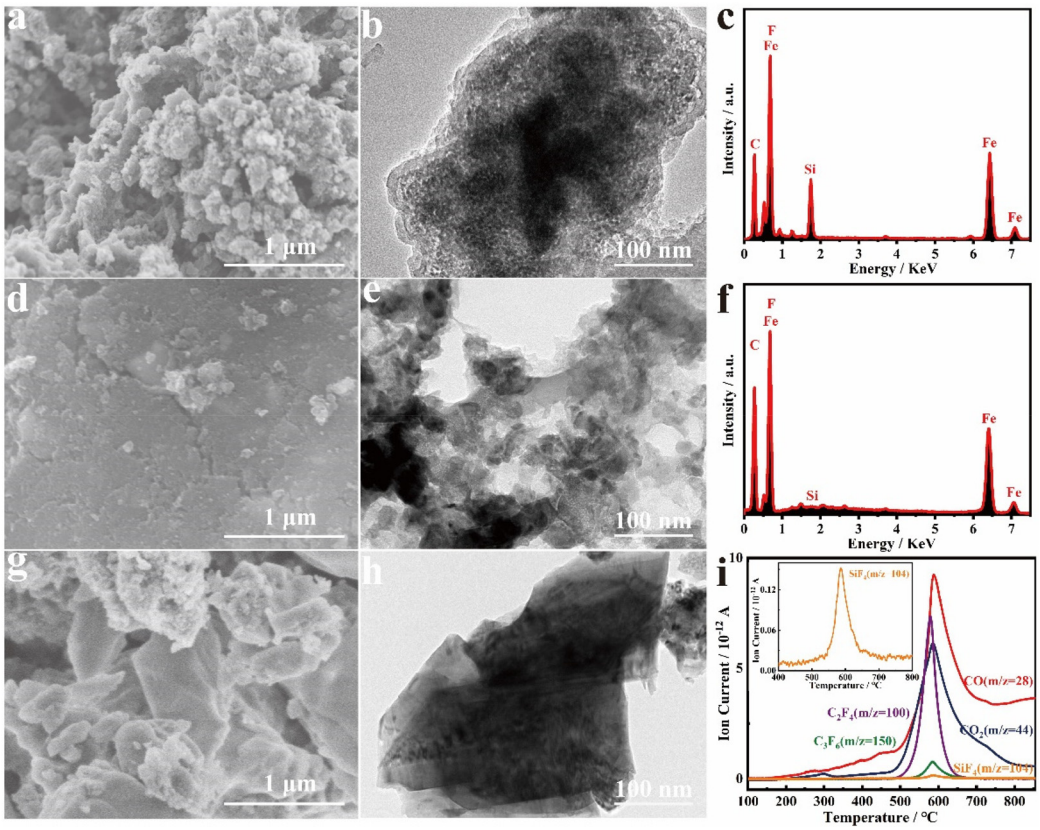

Fig. 3 (a) SEM image, (b) TEM image, and (c) EDX spectrum of the product obtained by the mass ratio of PTFE/Fe_2O_3@SOP = 3 : 1. (d) SEM image, (e) TEM image, and (f) EDX spectrum of the product obtained by the mass ratio of PTFE/Fe_2O_3@SOP = 10 : 1. (g) SEM image, and (h) TEM image of the product obtained under 800 °C. (i) Gas emission curves of PTFE and Fe_2O_3@SOP mixture during the pyrolysis process.

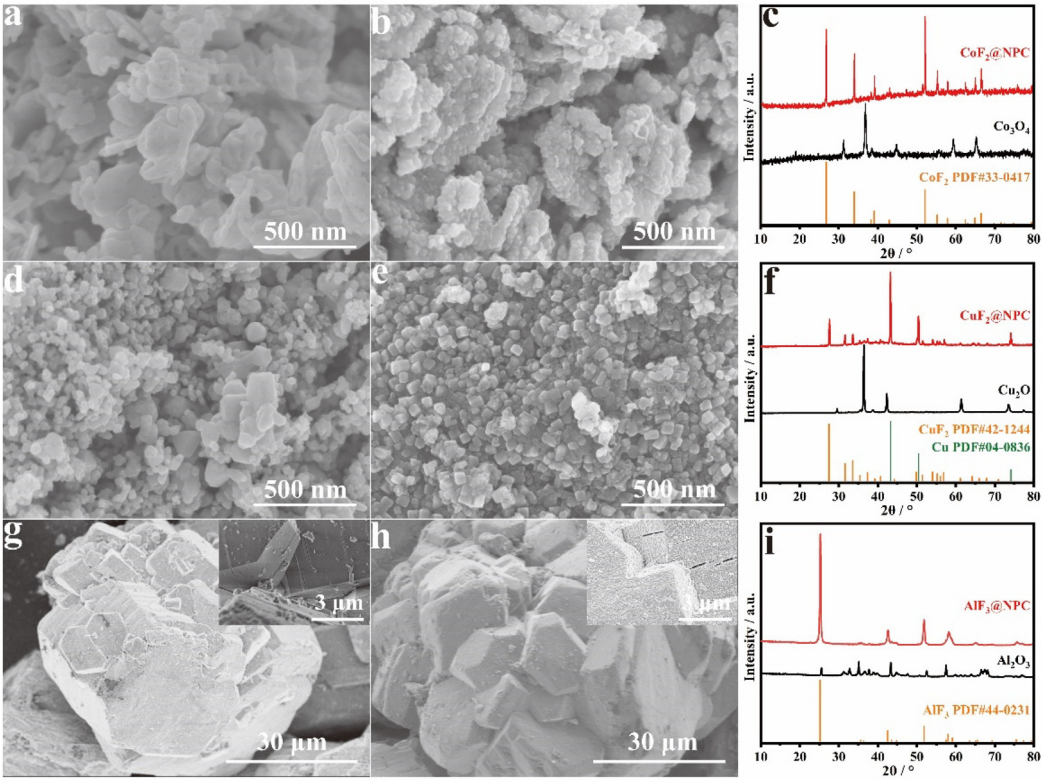

Fig. 4 (a) SEM image of Co_3O_4, (b) SEM image, and (c) XRD patterns of CoF_2@NPC. (d) SEM image of Cu_2O, (e) SEM image, and (f) XRD patterns of CuF_2@NPC. (g) SEM image of Al_2O_3. (h) SEM image and (i) XRD patterns of AlF_3@NPC.

excellent electrochemical stability of FeF_3@NPC. The cycling performance of FeF_3@NPC and commercial FeF_3 cathodes is presented in Fig. 5b. The FeF_3@NPC cathode delivers excellent specific capacities of 249 and 203 mA h g^{-1} at 0.2 C over 1 and 100 cycles, respectively. In contrast, the commercial FeF_3 cathode suffers significant capacity decay, and only maintains a low capacity of 29 mA h g^{-1} over 100 cycles, attributable to poor mechanical and interfacial stability. In addition, the specific capacity of the NPC cathode is only 16 mA h g^{-1} over 100 cycles (Fig. S8†), revealing that the capacity contribution of NPC can be negligible. Compared with reported FeF_3 cathode materials, the FeF_3@NPC cathode showcases comparable or better electrochemical properties (Table S1†). The rate capability of the FeF_3@NPC cathode is presented at different C-rates (Fig. 5c/d). At varying C-rates from 0.2 to 5 C, the FeF_3@NPC cathode exhibits high specific capacities of 229, 218, 205, 193, and 181 mA h g^{-1}, respectively. As the current returns to 0.2 C, a high reversible capacity of 221 mA h g^{-1} can be recovered. In sharp contrast, the commercial FeF_3 cathode delivers ultralow capabilities of 63, 44, 27, 18, and 9 mA h g^{-1}, respectively, signifying the outstanding rate capability of FeF_3@NPC. This good rate performance proves the improved electrochemical kinetics and rapid electronic/ionic transport characteristics of FeF_3@NPC, which can be buttressed by the relatively low charge-transfer resistance (R_{ct}) (Fig. S9†). The long cycle life of the FeF_3@NPC cathode was evaluated at 2 C (Fig. 5g). The FeF_3@NPC cathode preserves a stable reversible capacity of 172 mA h g^{-1} over 500 cycles of charge/discharge, corresponding to a superior capacity retention of 86.9% and a low capacity decay of 0.026% $cycle^{-1}$, accompanied by an almost 100% coulombic efficiency, evidencing the structural advantage of FeF_3@NPC.

The integrity of the FeF_3@NPC cathode after cycling was investigated with the postmortem SEM analysis (Fig. 6a/b and S10†). After the cycling test, the FeF_3@NPC cathode well maintains its original morphology without cracks, revealing the structural integrity of the cathode. The elemental analysis and TEM image of the cycled FeF_3@NPC cathode (Fig. 6c/d) show that the C, F and Fe elements are still homogeneously distributed in the carbon conduction network, and the N-doped porous carbon shell surrounding the FeF_3 nanoparticles remains intact, further indicating good robustness of the cathode and effective prevention of FeF_3 dissolution into the electrolyte. Compared to the FeF_3@NPC cathode before cycling, the thickness variation of the cycled FeF_3@NPC cathode is only 11.2% (Fig. 6e/f), implying that the well-constructed FeF_3@NPC nanocomposite can effectively accommodate severe volume fluctuation of FeF_3. Thus, the resulting FeF_3@NPC/Li batteries present excellent lithium storage performance.

To investigate the electrochemical kinetics of the FeF_3@NPC cathode, CV curves at different scanning rates (0.2,

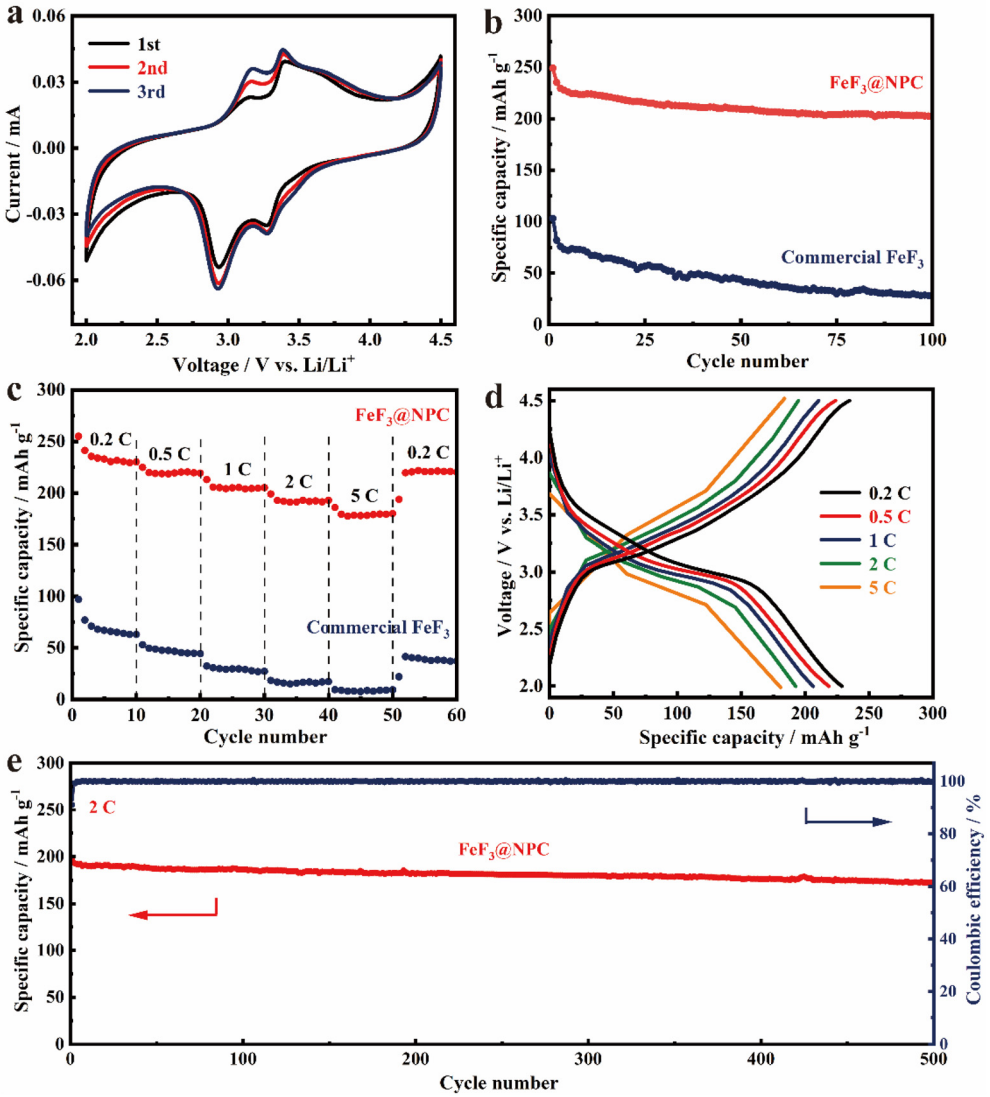

Fig. 5 (a) CV curves of FeF_3@NPC at 0.2 mV s^{-1}. (b) Cycling performance of FeF_3@NPC and commercial FeF_3 at 0.2 C. (c) Rate performance of FeF_3@NPC and commercial FeF_3 at different rates from 0.2 C to 5 C. (d) Voltage profiles of FeF_3@NPC at different current densities. (e) Long-term cycling performance of FeF_3@NPC at 2 C.

0.3, 0.4, 0.5, 0.6, 0.7, 0.8, and 0.9 mV s^{-1}) are presented in Fig. 7a. All the CV curves maintain the same trend, and the redox current intensity increases with the upswing of scanning rates, demonstrating the reversibility of the electrochemical conversion reaction for the FeF_3@NPC cathode.[20] Moreover, the slight redox peak shifts imply that the FeF_3@NPC cathode possesses fast kinetics. The relationship between the current (i) and the scanning rate (v) obeys eqn (1) and (2):[35]

$$i = av^b \quad (1)$$

$$\log(i) = b\log(v) + \log(a) \quad (2)$$

where b represents the Li^+ storage coefficient. The log(v) − log (i) plots of the FeF_3@NPC cathode (Fig. 7b) show that the calculated b-values of the anodic and cathodic peaks are 0.82 and 0.67, indicating considerable capacitive characteristics of FeF_3@NPC. The contribution rate of Li^+ capacitance can be quantified through eqn (3):[36]

$$i(V) = k_1v + k_2v^{1/2} \quad (3)$$

where $i(V)$ represents the combination of capacitive contribution (k_1v) and diffusion-controlled contribution ($k_2v^{1/2}$). A typical capacitive contribution at 0.9 mV s^{-1} is presented in Fig. 7c, and the variation of capacitive contribution and diffusion contribution under different scanning rates for FeF_3@NPC is shown in Fig. 7d. Obviously, as the scanning rates increase, the capacitive contribution rises gradually, accompanied by reduced diffusion contribution. The pseudocapacitive contribution of the FeF_3@NPC cathode can reach up to 75%. The superior pseudocapacitive properties facilitate

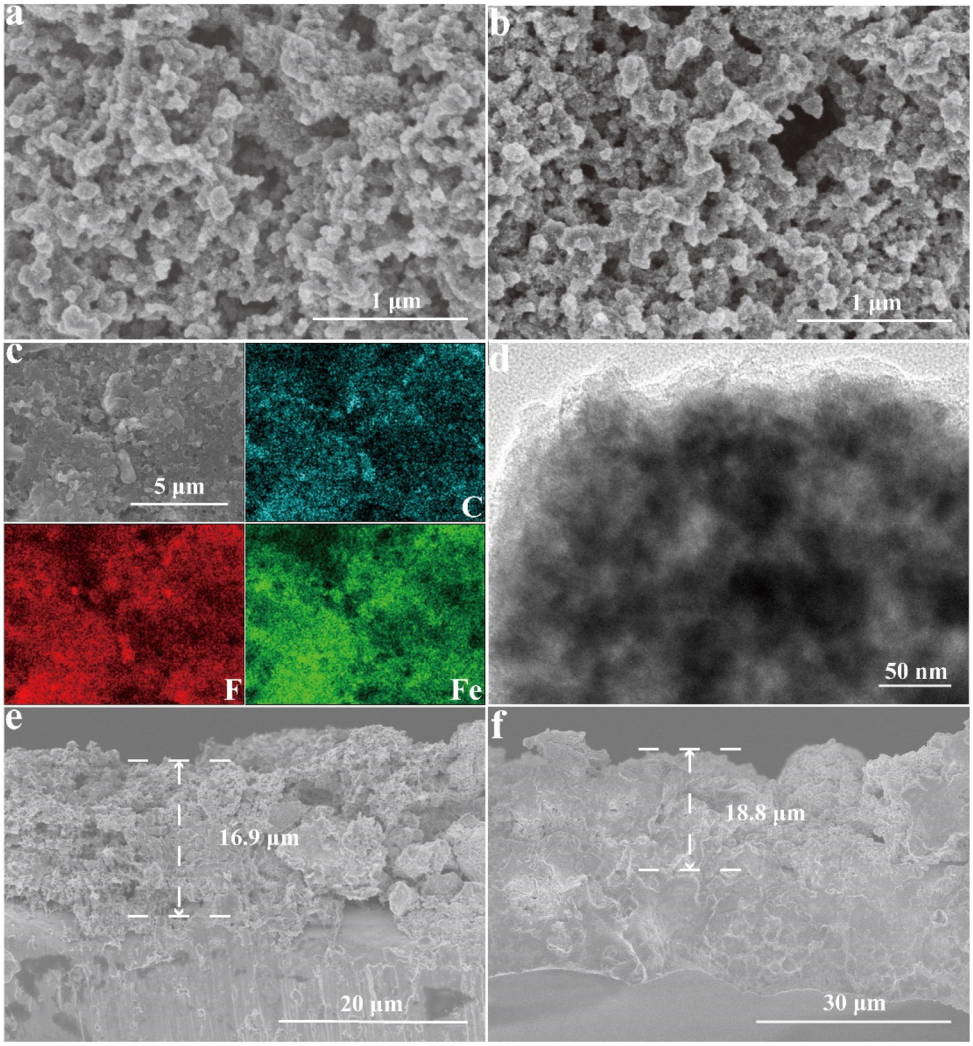

Fig. 6 (a and b) SEM images of the FeF_3@NPC cathode before and after 100 cycles. (c) EDS elemental mappings, and (d) TEM image of the FeF_3@NPC cathode after 100 cycles. (e and f) Cross-sectional SEM images of the FeF_3@NPC cathode before and after 100 cycles.

fast Li^+ storage, thus endowing the FeF_3@NPC cathode with outstanding cycle life and high-rate capability.

Experimental

Chemicals and materials

Polytetrafluoroethylene (PTFE), Fe_2O_3 powder, Co_3O_4 powder, Cu_2O powder, Al_2O_3 powder, glutaraldehyde solution (50% in H_2O), 3-aminopropyltriethoxysilane (APTES), commercial FeF_3, *N*-methyl pyrrolidone (NMP), and polyvinylidene fluoride (PVDF) were purchased from Aladdin (China). Acetylene black (AB) was offered from Guangzhou Lithium Force Energy Technology Co. (China), commercial electrolyte using EC/DMC/DEC (v/v/v = 1 : 1 : 1) solvent with 1 M $LiPF_6$ was purchased from Shanghai Xiaoyuan Energy Technology Co. (China).

Synthesis of Fe_2O_3@SOP

APTES (2.66 g, 12.0 mmol) and Fe_2O_3 (2.87 g, 18.0 mmol) were placed in a 500 mL glass bottle with C_2H_5OH/H_2O (v/v = 60 mL : 240 mL) and stirred for 1 h. Then, glutaraldehyde solution (50% in H_2O, 2.40 g, 12.0 mmol) was added dropwise and kept under vigorous stirring for 6 h. The precipitate was washed with C_2H_5OH/H_2O and subsequently dried at 80 °C, yielding a Schiff-base organic precursor containing Fe_2O_3, *i.e.*, Fe_2O_3@SOP.

Synthesis of FeF_3@NPC

0.5 g of Fe_2O_3@SOP and 3.0 g of PTFE powder were well ground for 0.5 h, and then calcined at 650 °C for 4 h under an Ar atmosphere to obtain FeF_3@NPC. Other NPC-confined metal fluorides were synthesized *via* the same procedures with different metallic oxides.

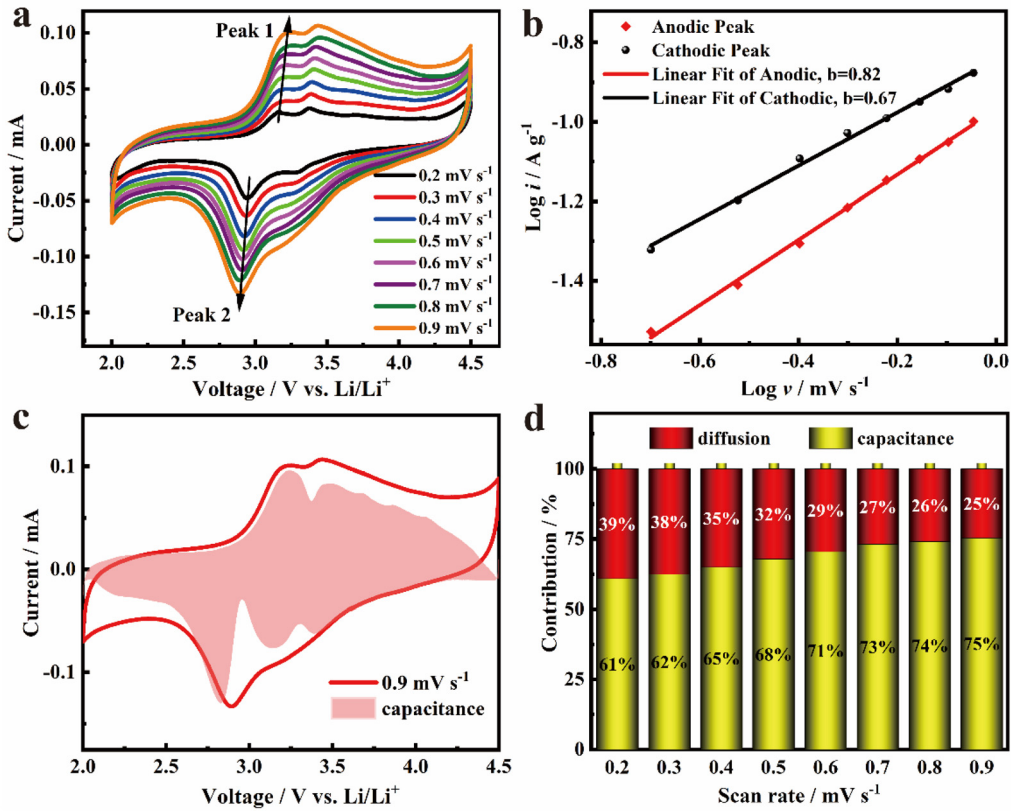

Fig. 7 (a) CV curves at different scanning rates; (b) the fitted *b* values determined by the peak current and scanning rate; (c) schematic diagram of the capacitive contribution at 0.9 mV s^{-1}; and (d) capacity contribution ratio at various scanning rates of FeF_3@NPC.

Material characterization

The surface morphology, elemental mapping, and microstructure characterization were analyzed using a transmission electron microscope (TEM, Hitachi S-4800) and a scanning electron microscope (SEM, Hitachi S-4800). The chemical states were collected using an X-ray photoelectron spectrometer (XPS, ESCALAB250). The conductivity was measured using a four-point probe instrument (RTS-9). FTIR spectra were recorded using a Nicolet iS50. The crystal structures were obtained using an X-ray diffractometer (XRD, X'Pert Pro MPD) and a Raman spectrometer (HORIBA Jobin Yvon). The N_2 adsorption isotherm and pore-size distribution were tested on an SI-MP-10. Pyrolysis characteristics were analysed on a TG-MS analyzer (STA449 F3). Thermogravimetric analysis (TGA) was performed using a PCPFEIFFER VACUUMTGA-7 analyzer.

Electrochemical measurement

To prepare the electrode, a mixture of 80 wt% FeF_3@NPC or commercial FeF_3, 10 wt% acetylene black (AB) conductive agent, and 10 wt% polyvinylidene fluoride (PVDF) binder in *N*-methyl pyrrolidone (NMP) was cast on aluminum foil and dried at 90 °C for 12 h. The FeF_3 mass loading was approximately 1.2–1.6 mg cm^{-2}. A 2025-type coin cell assembly was conducted inside an Ar-filled glovebox (Mikrouna) by using FeF_3@NPC or commercial FeF_3 as the cathode, lithium sheet as the anode, polypropylene membrane as the separator, and 1 M $LiPF_6$/EC : DMC : DEC (v/v/v = 1 : 1 : 1) as the electrolyte. Cyclic voltammetry (CV) measurements (0.2 mV s^{-1}, 2.0–4.5 V) and electrochemical impedance spectroscopy (EIS) measurements (0.01 Hz to 0.1 MHz) were recorded using a Zahner IM6 electrochemical workstation. The galvanostatic discharge/charge tests were conducted using a Neware multichannel battery system. The electrochemical capacities of the electrodes were based on the mass of FeF_3.

Conclusions

In summary, an innovative *in situ* synthetic approach is proposed to make N-doped porous carbon-confined metal fluorides. The afforded FeF_3@NPC with a confined N-doped carbon-coated space can facilitate fast Li^+/e^- diffusion kinetics, buffer severe volume fluctuation and prevent the active substance FeF_3 from interacting with the electrolyte, thus enabling a high capacity utilization of 249 mA h g^{-1} at 0.2 C, together with remarkable C-rate capability and excellent cycle life. This work opens up an efficient pathway for developing nanocon-

fined metal fluoride-based materials to improve lithium batteries.

Author contributions

Jinlong Hu: conceptualization, methodology, investigation, formal analysis, writing – original draft, and writing – review & editing. Weijun Xu: resources and software. Lingzhi Zhang: supervision and writing – review & editing.

Data availability

The data supporting this article have been included as part of the ESI.†

The data that support the findings of this study are available from the corresponding author upon reasonable request.

Conflicts of interest

There are no conflicts to declare.

Acknowledgements

This study was supported by the Key-Area Research and Development Program of Guangdong Province under Grant (2023B0909060004) and Dongguan Municipal Key R&D Program (20221200300112).

References

1 F. Wu, J. Maier and Y. Yu, *Chem. Soc. Rev.*, 2020, **49**, 1569–1614.
2 F. X. Wu, V. Srot, S. Q. Chen, M. Y. Zhang, P. A. Aken, Y. Wang, J. Maier and Y. Yu, *ACS Nano*, 2021, **15**, 1509–1518.
3 S. S. Xiao, P. T. Sun, Y. Y. Xie, X. G. Zhou, Y. Li and L. Y. Wang, *J. Mater. Chem. A*, 2024, **12**, 20783–20802.
4 E. Zhao, O. Borodin, X. S. Gao, D. Lei, Y. R. Xiao, X. L. Ren, W. B. Fu, A. Magasinski, K. Turcheniuk and G. Yushin, *Adv. Energy Mater.*, 2018, **8**, 1800721.
5 X. J. Xu, F. K. Li, D. C. Zhang, S. M. Ji, Y. P. Huo and J. Liu, *Mater. Chem. Front.*, 2022, **6**, 3512–3521.
6 W. W. Zhang, B. Song, M. L. Wang, T. T. Miao, X. L. Huang, E. H. Zhang, X. W. Zhan, Y. Yang, H. Zhang and K. Lu, *Energy Environ. Sci.*, 2024, **17**, 5273–5282.
7 W. T. Gu, O. Borodin, B. Zdyrko, H. T. Lin, H. Kim, N. Nitta, J. X. Huang, A. Magasinski, Z. Milicev, G. Berdichevsky and G. Yushin, *Adv. Funct. Mater.*, 2016, **26**, 1507–1516.
8 L. P. Li, J. H. Zhu, M. W. Xu, J. Jiang and C. M. Li, *ACS Appl. Mater. Interfaces*, 2017, **9**, 17992–18000.
9 C. L. Li, L. Gu, J. W. Tong, S. Tsukimoto and J. Maier, *Adv. Funct. Mater.*, 2011, **21**, 1391–1397.
10 Y. S. Shi, X. Z. Xu, J. Li, J. Y. Li, P. P. Yin, Q. T. Jiang, J. J. Wang, W. B. Li, K. H. Xu, K. Zhang, J. Yang and X. F. Li, *ACS Appl. Mater. Interfaces*, 2023, **15**, 41504–41515.
11 Y. J. Wang, P. Zhou, M. Y. Zhang, Z. J. He, Y. Cheng, Y. Zhou and F. X. Wu, *Energy Storage Mater.*, 2023, **60**, 102847.
12 H. Jung, J. Shin, C. Chae, J. K. Lee and J. Kim, *J. Phys. Chem. C*, 2013, **117**, 14939–14946.
13 F. Badway, N. Pereira, F. Cosandey and G. G. Amatucci, *J. Electrochem. Soc.*, 2003, **150**, 1209–1218.
14 J. Ding, X. Y. Zhou, C. C. Luo, H. R. Xu, J. Yang and J. J. Tang, *J. Mater. Sci.*, 2022, **57**, 1261–1270.
15 T. Kim, W. J. Jae, H. Kim, M. Park, J. M. Han and J. Kim, *J. Mater. Chem. A*, 2016, **4**, 14857–14864.
16 L. Sun, Y. Li and W. Feng, *Small Methods*, 2023, **7**, 2201152.
17 W. T. Gu, A. Magasinski, B. Zdyrko and G. Yushin, *Adv. Energy Mater.*, 2015, **5**, 1401148.
18 Y. S. Shi, P. P. Yin, J. Li, X. Z. Xu, Q. T. Jiang, J. Y. Li, H. M. K. Sari, J. J. Wang, W. B. Li, J. H. Hu, Q. X. Lin, J. Q. Liu, J. Yang and X. F. Li, *Nano Energy*, 2023, **108**, 108181.
19 Q. Zhang, X. Wu, S. Gong, L. S. Fan and N. Q. Zhang, *ChemistrySelect*, 2019, **4**, 10334–10339.
20 Q. X. Cheng, Y. Y. Pan, Y. Y. Chen, A. Zeb, X. M. Lin, Z. Z. Yuan and J. C. Liu, *Inorg. Chem.*, 2020, **59**, 12700–12710.
21 J. L. Hu and L. Z. Zhang, *J. Mater. Chem. A*, 2021, **9**, 27560.
22 J. Li, L. Fu, J. Zhu, W. Yang, D. Li and L. Zhou, *ChemElectroChem*, 2019, **6**, 5203–5210.
23 H. Wang, B. Hou, Y. Yang, Q. Chen, M. Zhu, A. Thomas and Y. Liao, *Small*, 2018, **14**, 1803232.
24 K. Du, R. Tao, C. Guo, H. F. Li, X. L. Liu, P. M. Guo, D. Y. Wang, J. Y. Liang, J. L. Li, S. Dai and X. G. Sun, *Nano Energy*, 2022, **103**, 107862.
25 H. Jung, J. Shin, C. Chae, J. K. Lee and J. Kim, *J. Phys. Chem. C*, 2013, **117**, 14939–14946.
26 J. Yang, Z. Xu, H. Zhou, J. Tang, H. Sun, J. Ding and X. Zhou, *J. Power Sources*, 2017, **363**, 244–250.
27 X. Zhou, H. Sun, H. Zhou, Z. Xu and J. Yang, *J. Alloys Compd.*, 2017, **723**, 317–326.
28 X. Li, Y. Zhang, Y. Meng, G. Tan, J. Ou, Y. Wang, Q. Zhao, H. Yuan and D. Xiao, *ChemElectroChem*, 2017, **4**, 1856–1862.
29 W. Fu, E. Zhao, Z. Sun, X. Ren, A. Magasinski and G. Yushin, *Adv. Funct. Mater.*, 2018, **28**, 1801711.
30 H. Zhang, M. L. Wang, B. Song, X. L. Huang, W. L. Zhang, E. H. Zhang, Y. W. Cheng and K. Lu, *Angew. Chem., Int. Ed.*, 2024, **63**, e202402274.
31 Z. X. Pei, H. F. Li, Y. Huang, Q. Xue, Y. Huang, Z. F. Wang and C. Y. Zhi, *Energy Environ. Sci.*, 2017, **10**, 742–749.
32 Y. Q. Shen, X. Y. Wang, H. Hu, M. L. Jiang, X. K. Yang and H. B. Shu, *J. Power Sources*, 2015, **283**, 204–210.
33 X. Fan, Y. Zhu, C. Luo, L. Suo, Y. Lin, T. Gao, K. Xu and C. Wang, *ACS Nano*, 2016, **10**, 5567–5577.

34 J. Li, L. C. Fu, Z. W. Xu, J. J. Zhu, W. L. Yang, D. Li and L. P. Zhou, *Electrochim. Acta*, 2018, **281**, 88–98.
35 Z. Jiang, Y. J. Wang, X. F. Chen, F. L. Chu, X. S. Jiang, F. Kwofie, Q. Pei, S. Luo, J. Arbiol and F. X. Wu, *J. Mater. Chem. A*, 2023, **11**, 21541–21552.
36 X. Hua, A. S. Eggeman, E. Castillo-Martínez, R. Robert, H. S. Geddes, Z. Lu, C. J. Pickard, W. Meng, K. M. Wiaderek, N. Pereira, G. G. Amatucci, P. A. Midgley, K. W. Chapman, U. Steiner, A. L. Goodwin and C. P. Grey, *Nat. Mater.*, 2021, **20**, 841–850.